AGU100 ADVANCING EARTH AND SPACE SCIENCE

JGR Planets

RESEARCH ARTICLE
10.1029/2018JE005837

Key Points:
- We apply a proposed paleoshoreline-identification toolkit to newer high-resolution data of an exemplar site for paleoshorelines on Mars
- Any wave-generated paleoshorelines should exhibit expressions identifiable in the residual topography from an idealized slope
- Our analysis of these curvilinear features does not support a paleoshoreline interpretation and is more consistent with eroded lithologies

Supporting Information:
- Supporting Information S1

Correspondence to:
S. F. Sholes,
sfsholes@uw.edu

Citation:
Sholes, S. F., Montgomery, D. R., & Catling, D. C. (2019). Quantitative high-resolution reexamination of a hypothesized ocean shoreline in Cydonia Mensae on Mars. *Journal of Geophysical Research: Planets*, *124*, 316–336. https://doi.org/10.1029/2018JE005837

Received 24 SEP 2018
Accepted 15 JAN 2019
Accepted article online 21 JAN 2019
Published online 7 FEB 2019

Quantitative High-Resolution Reexamination of a Hypothesized Ocean Shoreline in Cydonia Mensae on Mars

Steven F. Sholes[1,2], **David R. Montgomery**[1], **and David C. Catling**[1,2]

[1]Department of Earth and Space Sciences, University of Washington, Seattle, WA, USA, [2]Astrobiology Program, University of Washington, Seattle, WA, USA

Abstract Primary support for ancient Martian oceans has relied on qualitative interpretations of hypothesized shorelines on relatively low-resolution images and data. We present a toolkit for quantitatively identifying paleoshorelines using topographic, morphological, and spectroscopic evaluations. In particular, we apply the validated topographic expression analysis of Hare et al. (2001, https://doi.org/10.1029/2001JB000344) for the first time beyond Earth, focusing on a test case of putative shoreline features along the Arabia level in northeast Cydonia Mensae, as first described by Clifford and Parker (2001, https://doi.org/10.1006/icar.2001.6671). Our results show these curvilinear features are inconsistent with a wave-generated shoreline interpretation. The topographic expression analysis identifies a few potential shoreline terraces along the historically proposed contacts, but these tilt in different directions, do not follow an equipotential surface (even accounting for regional tilting), and are not laterally continuous. Lineaments appear blocky in nature at small scales, and they bifurcate, truncate, and merge along track. These features are more consistent with material boundaries for lithological units exposed along a degraded crater wall. These results do not preclude the existence of an ancient hemispheric ocean, but the geophysical and high-resolution topographic data at this site do not support such an interpretation.

Plain Language Summary There is an ongoing controversy about whether Mars had ancient oceans. Abundant evidence for past surface liquid water exists, but it is debated how much and for how long it persisted on Mars' surface. Features have previously been traced out in relatively low-resolution images and interpreted as shorelines of episodic ancient oceans. However, new high-resolution data allow for better and more complete analyses. Here we present methods to determine whether any proposed ancient shoreline feature meets the requirements to be classified as a shoreline using these improved data. Shorelines should form flat "step-like" landforms at a near-constant elevation, so one critical analysis looks at the shape and elevation of proposed features. We examine a site that has been promoted in the literature as an exemplar of ancient shorelines and find that this site lacks a diagnostic shoreline shape. Instead, features at this site are better explained as exposed and eroded rock layers that mimic shoreline shapes in low-resolution images. Our findings do not mean that oceans never existed on Mars, only that this specific site does not support the ocean hypothesis. Application of our methods to similar sites could shed further light on the ocean hypothesis.

1. Introduction

The extent and duration of large open reservoirs of liquid water on the surface of Mars are some of the most intriguing questions about the planet's past. Support for vanished oceans historically stems from the recognition that large outflow channels and valley networks empty into the northern plains, suggesting these lowlands served as a basin where water pooled (Baker et al., 1991; Jöns, 1985; Lucchitta et al., 1986). These observations, coupled with hand-mapped contacts along the edges of the northern plains on comparatively low-resolution images, led to the interpretation of these contacts as paleoshorelines (Parker et al., 1989, 1993). The question of whether or not such an ocean (or oceans) existed has profound implications for the past climate of Mars (e.g., Banfield et al., 2015; Jakosky & Phillips, 2001; Lammer et al., 2018; Ramirez & Craddock, 2018), the possibility of the planet harboring ancient life (e.g., Beaty et al., 2005), and the evolution and role of liquid water in its surficial geology (e.g., Carr & Head, 2010, 2015).

Two distinct contacts identified by Parker et al. (1989, 1993) were described roughly following the topographic dichotomy along the northern plains boundary and interpreted as corresponding to different hypothesized ocean highstands. The Arabia level ("contact 1") roughly follows the dichotomy transition region and represents a hypothesized larger and older ocean stand. The Deuteronilus level ("contact 2") is an inner contact almost entirely within the northern plains thought to represent a smaller and younger ocean stand (Parker et al., 1989, 1993). Additional possible discontinuous shorelines have been proposed, along with the "Meridiani Contact" that extends beyond the dichotomy boundary into the southern highlands and would represent a much larger and earlier ocean stand (Edgett & Parker, 1997).

Initial identification of these hypothesized shorelines was based on the best available high-resolution *Viking* images (~10 m per pixel) with most of the contacts mapped at comparatively lower resolutions (~50–200 m per pixel; Clifford & Parker, 2001; Parker et al., 1989, 1993). Later interpolation of these contacts onto Mars Orbiter Laser Altimeter (MOLA) topographic data (Smith et al., 2001) shows vast ranges in elevations of ~2.5 km for the Arabia contact (Carr & Head, 2003) and ~0.6 km for the Deuteronilus contact (Carr & Head, 2003; Ivanov et al., 2017). Such wide ranges in elevation for suspected equipotential surfaces cast doubt on a paleoshoreline interpretation. Misidentification along parts of the Arabia contact with the low-resolution *Viking* data may contribute up to ~2 km of the discrepancy (Parker & Calef, 2012), while some have invoked true polar wander and/or Tharsis-induced long-wavelength flexure as a means of deforming the shorelines to their present levels (N. H. Chan et al., 2018; Citron et al., 2018; Perron et al., 2007).

Since these contacts were first proposed, many studies have used them as evidence of past oceans on Mars despite near complete ambiguity in other lines of evidence relevant to assessing their existence. Studies have found that past Mars water inventories are both consistent with (Villanueva et al., 2015) and incompatible with (Carr & Head, 2015) an early ocean. Similarly, radar investigations into the underlying deposits under the northern plains show permittivity values argued to be in agreement with both vesicular lavas (Boisson et al., 2011) and sedimentary ocean remnants (Mouginot et al., 2012). Further investigations of these geomorphological contacts have similarly both supported and challenged a coastal origin for segments along both the Arabia and Deuteronilus contacts (e.g., Carr & Head, 2003; Parker et al., 2010). Many putative paleoshoreline locations exhibit landforms that more closely resemble features formed by other processes, such as lava flows and mass wasting events (Carr & Head, 2003; Ghatan & Zimbelman, 2006; Sholes et al., 2014).

Much of the recent focus on geomorphological evidence of shorelines has been placed on reconciling the discrepancies in the absolute elevations along the contacts with regional equipotential surfaces (e.g., N. H. Chan et al., 2018; Di Achille & Hynek, 2010; Parker & Calef, 2012; Parker et al., 2010). Apart from the occasional paper (e.g., studies of south Isidis by Erkeling et al., 2014, 2012), little research has been done to reexamine individual proposed shorelines using the latest available high-resolution data products. As the amount of data grows, it is important to reassess these regional contacts at the local level. This reassessment can test if broad-scale mechanistic interpretations are supported by the fine-scale geomorphological evidence.

Understanding the role and extent of past liquid water is especially crucial in determining the habitability of past Mars. Life, as we know it, requires liquid water, which cannot persist on the current surface of Mars under the cold, dry, and thin atmosphere. Analysis of closed-basin crater lakes suggests that they represent past transient bodies of liquid water (Goudge et al., 2015; Grotzinger et al., 2015) and there is evidence of a $>10^6$ km^2 liquid-water Eridania sea (Irwin et al., 2004, 2002). However, positive identification of wave-generated paleoshorelines could aid in constraining the paleobarometry of Mars' atmosphere (Banfield et al., 2015; Kraal et al., 2006) and indicate whether the climate was stable enough to prevent the geologically rapid dissipation of any oceans to create such landforms (Jakosky & Phillips, 2001). Long-lived periods of clement conditions and hydrologic cycling in the presence of an ocean have been proposed (Hynek et al., 2010). Oceans have also been proposed as aiding in the production of prebiotic chemistry (e.g., Stüeken et al., 2013). Thus, the presence, longevity, and magnitude of any putative ocean(s) are important habitable conditions on early Mars.

Here we present and apply a quantitative toolkit for resolving and characterizing landforms on Mars that are hypothesized to be paleoshorelines. We include classical tools such as spectral analysis, thermal inertia, and qualitative photogeologic mapping. But in addition, for the first time, we apply the topographic expression analysis (TEA) methodology used for quantitatively identifying and comparing wave-generated paleoshorelines on Earth (Hare et al., 2001; Jewell, 2016), to their suspected Martian counterparts. With the success of this methodology in identifying subtle intermittent paleoshorelines on Earth, we propose using TEA as a useful additional criterion for identifying extraterrestrial wave-generated paleoshoreline candidates. While the TEA method is unable to positively identify the genetic origin of the landforms due to the potential for false positives, recognizable and coherent terrace features should meet the criteria described below in their topographic signal (when they exist in the geomorphology). Thus, the combined approach using all the available tools presented here can aid in determining a probable origin.

Any Martian shorezones should be laterally continuous across the basin, and general opinion suggests that preserved wave-generated erosional shorelines should exhibit a bench or platform shape (M. A. Chan et al., 2016). Given the climatic uncertainty for past Mars, perennially ice-covered, or even completely frozen, oceans have been hypothesized (Carr & Head, 2019; Clifford & Parker, 2001), potentially limiting wave-generated coastal landforms. However, the amount of time for a convecting sea to freeze (Banfield et al., 2015; Carr, 1996) depends on the salinity, water depth, and climate, and some parameter combinations allow sufficient time to erode shoreline features (Clifford & Parker, 2001; Kreslavsky & Head, 2002). Even once frozen, potential seasonal breakup of thin shoreline ice may allow for wind-generated waves (Parker & Currey, 2001) under suitable climatic regimes and with sufficient wave energy (Banfield et al., 2015; Kraal et al., 2006). Otherwise, coastal processes along a permanently ice-capped sea would likely be subject to currents formed by stream input, ice-cover oscillations due to winds (creating standing-wave like currents), and heat transfer (Castendyk et al., 2015; Malm, 1999; Wharton et al., 1995).

Despite an abundance of newer high-resolution data, many of the proposed wave-generated shoreline “bench” features have been identified primarily upon a qualitative assessment in orbital imagery that has much lower spatial resolution (e.g., Viking, Thermal Emission Imaging Spectrometer [THEMIS], and Mars Orbiter Camera [MOC] wide angle) than currently available and quantitatively with limited low-resolution elevation data (i.e., MOLA). Little research has been done to reinvestigate these features with the new data. Thus, there is a growing need for both a reanalysis with higher-resolution data and better quantitative methods for defining and measuring these potential terrace features.

Ultimately, our approach provides a framework for testing the validity of hypothesized extraterrestrial wave-generated paleoshoreline contacts. Here we apply these methods to a proposed Martian paleoshoreline first described at depth in Clifford and Parker (2001; their Figure 4) at a site multiple sources have cited as having contacts strongly reminiscent of terrestrial strandlines (erosional features demarking equipotential water levels; Cabrol & Grin, 1999; Clifford & Parker, 2001; El Maarry et al., 2010; Parker, 2004; Parker et al., 2002, 2010; Sholes et al., 2014; Świąder, 2014; Webb, 2004).

1.1. Site Introduction

The site itself lies to the northeast of the Cydonia Mensae region along the topographic dichotomy and is centered at approximately 36.4°N, 350.2°E. It straddles the early Hesperian transition unit and the middle Noachian highland unit (Tanaka et al., 2014) along the older Arabia level with the Deuteronilus level only ~100 km north. Most studies have focused on the eastern-most crater (crater A) in a complex of three adjacent remnant craters ~50 km in diameter (see Figure 1). Hypothesized paleoshorelines have also been identified locally along crater B's western rim (Parker et al., 2010). Parts of the crater rim septa separating the craters have been eroded away and the northeast section of crater A and the northwest section of crater C are also opened, exposing the craters' interiors to the northern plains. Thus, depending on the timing of these breaches, these hypothesized paleoshorelines potentially could be the result of either a crater lake or a northern ocean. We focus primarily on crater A (the easternmost crater) given multiple targeted high-resolution stereo pair imagery available for that area (white boxes in Figure 1).

Interpretation of these features as paleoshorelines largely hinged on numerous visually identified subtle arcuate ridges that follow the dissected margin of the highlands. These ridges were interpreted by Clifford and Parker (2001) as constructional coastal barrier ridges, while other visible arcuate lineaments were interpreted as possible strandlines. Later assessments by Ghatan and Zimbelman (2006) claimed that these ridges were more likely created by interstitial-ice-creep deformation (Squyres, 1979; Squyres & Carr, 1986), eolian processes, or debris-covered glaciers (Levy et al., 2010) based on similar features found in a nearby

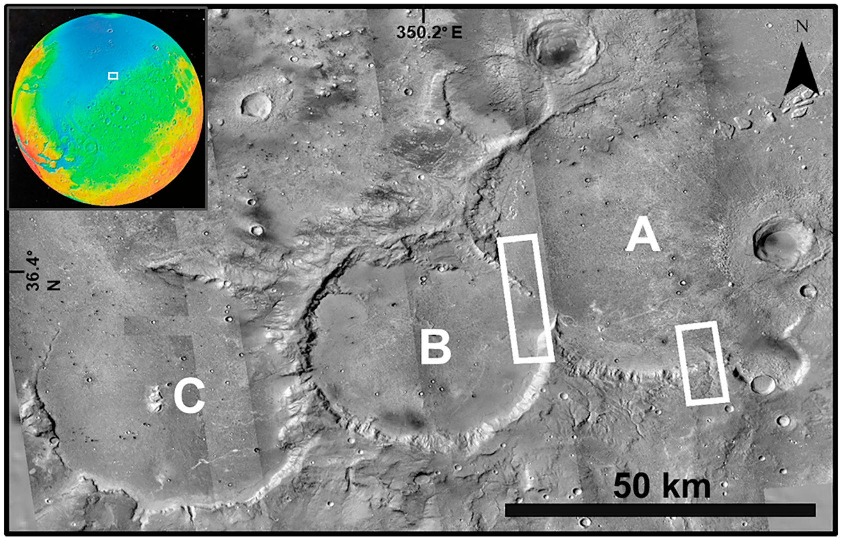

Figure 1. Context Camera mosaic of the three-crater system (centered three largest craters labeled A–C) to the NE of Cydonia Mensae showing the selected test site region. The center of the image is approximately 36.4°N, 350.2°E. White boxes indicate digital elevation model footprints from High Resolution Imaging Science Experiment stereo pairs for the western and southern sites. The crater complex is open to the northern plains (and thus a potential ocean) on the NE side of crater A and NW side of crater C. (inset) Mars Orbiter Laser Altimeter colorized elevation showing the site (white box) in relation to the topographic dichotomy (which roughly follows the blue/green boundary on the globe).

enclosed crater (i.e., one not open to the northern plains). However, since then, the *Mars Reconnaissance Orbiter* has acquired a wealth of high-resolution data and allowed production of submeter elevation data. These data products allow for a more complete and thorough analysis of the site than was otherwise possible, especially given the typically narrow extent of both constructional and erosional coastal landforms.

Crater floor polygons have also been identified within the base of crater A and used in support for a paleolake interpretation (Cabrol & Grin, 1999; El Maarry et al., 2010). These polygons typically occur in crater infill material and are usually interpreted as the result of thermal stress and periglacial processes; though water ice is expected to be unstable at these lower latitudes today (Clifford et al., 2010; Mellon et al., 1997). Modeling suggests they can instead be ancient crater lake desiccation polygons. However, both past climatic variations, caused by changes in obliquity, and desiccation of crater lake sediments can account for the observed ~40 m diameter polygons (El Maarry et al., 2010) leaving an ambiguous interpretation as to their origin.

2. Methods

2.1. Photogeological Mapping

We map geomorphic features using ArcGIS (www.esri.com) for the sites of interest (where paleoshoreline features have been proposed) identifying key landforms and units to determine a likely formational mechanism. We focus on using available High Resolution Imaging Science Experiment (HiRISE) images as they provide the greatest detail at ~30–50 cm per pixel (McEwen et al., 2007). However, HiRISE data have small surface footprints and limited global coverage, so Context Camera (CTX) images (~6 m per pixel, nearly global coverage) are used for regional mapping and supplementing local HiRISE coverage (Malin et al., 2007). Since many of the putative contacts have previously been investigated with resolutions comparable to CTX images (e.g., Clifford & Parker, 2001; Ghatan & Zimbelman, 2006; Parker et al., 2010), much more emphasis here is placed on characterizing the lineaments with available HiRISE data. This includes testing for lateral continuity.

Contacts previously published in the literature are mapped, as are any additional contacts that arise in examining the higher-resolution data. After locating the candidate paleoshoreline contacts, we mapped and described characteristic landforms that are locally adjacent or congruent with the contacts. Table 1

Table 1

Necessarily Abbreviated List of Typical Landforms and Their Associated Characteristic Features Used for Identifying the Origin of Contacts That May Be Shorelines in the Case of Coastal Features or May Mimic Shorelines in the Case of Other Landforms

Volcanic	Glacial	Coastal	Impact	Other
Overlapping lobate flows	Lobate flows	Coastal bluffs/cliffs	Craters	Fault escarpments
Destroyed craters	Contact scouring	Strandlines	Ejecta blankets	Albedo contacts
Lava tubes	Debris aprons	Marine terraces	Melt flows	Lithological contacts
Pressure ridges (perpendicular to flow direction)	Flow lineaments (in direction of flow)	Beaches, berms, and arcuate beach ridges	Concentric lineaments	Colluvium and mass wasting features
Rocky terrain	Moraines	Deltas		
Dark color (basaltic?)	Drumlins, erratics, and eskers	Barrier islands, spits, and tombolos		
Resistant cap rocks	U-shaped valleys	Sea stacks		
Terminus slopes downward	Terminus slopes downward	Ocean slopes upward to shore		
High lava marks (from lava drainage)	Pressure ridges (perp. to flow)	Pillow basalt transitions		

Note. While by no means exhaustive, the table provides a useful overview.

provides a necessarily incomplete list of possible characteristic landforms and their associated formational processes which we have lumped into five broad formational categories, including coastal landforms that define true shorelines (both from open and ice-covered seas), and four categories that can mimic shoreline-like contacts: volcanic, glacial, impact, and “other” (e.g., diffuse albedo contacts and mass-wasting features).

The difficulty in qualitative photogeological mapping lies in the (1) overlap between landforms formed through vastly different processes and (2) their unknown preservation potential over billions of years. This difficulty often forces a subjective interpretation (e.g., barrier ridges, ice-shoved ridges, and volcanic and glacial pressure ridges). Arguably some of the best features to identify paleoshorelines would be exposed subaerial lava flows that progress into pillow basalts such as subaerial-to-subaqueous transitions found in terrestrial geology even as far back as in Archean rocks (e.g., Som et al., 2016). Pillows, however, are unlikely to be observable even with modern high-resolution images but could be identified with future missions. While megapillows would be easier to observe and have been identified on Earth, they are much rarer than typical pillow basalts and not as densely packed (Bear & Cas, 2007; Walker, 1992).

2.2. Topographic Analysis

2.2.1. DEMs

Many common landforms have distinct topographic expressions that aid in their identification. MOLA data have typically been used in the past as they have nearly global coverage, but at ~400–500 m per pixel binned lateral resolution (and ~300 m N-S along-track altimetry shot spacing), it is too coarse for studying narrow features but is useful for studying regional trends. Digital elevation models (DEMs) have been made available for many of the High Resolution Stereo Camera (HRSC) stereo pair images (Jaumann et al., 2007). These HRSC DEMs have better spatial resolution at ~75 m per pixel but at the expense of vertical resolution.

Typical terrestrial nontidal shorezone topographic features (e.g., lacustrine wave-cut terraces not subject to terrestrial oceanic-scale tides, modulated by fetch, wind-speed, atmospheric pressure, and local shore geometry) are on the order of tens of meters wide (or less), thus, MOLA and HRSC DEMs are ill-equipped to accurately identify them. To get submeter resolution DEMs, we use the open source NASA Ames Stereo Pipeline (ASP; Moratto et al., 2010; Öhman, 2013; Shean et al., 2016) to perform automated photogrammetry on HiRISE stereo pair images located at each site. This produces DEMs with typically 1–2 m per pixel spatial resolution and ~1 m vertical resolution. Where HiRISE stereo pair images are unavailable, CTX and MOC narrow angle stereo pairs (and some overlapping CTX images, given sufficient illumination angles and viewing geometries) can also be used with ASP to create DEMs with resolutions as good as ~6 m per pixel (Öhman, 2013; Tao et al., 2018). In the absence of images suitable for photogrammetry, MOLA Precision Experiment Data Record (PEDR) data products offer individual altimetry shot readings.

The resulting DEM is checked for artifacts using ASP-outputted masks. Some areas, typically places that are featureless or with steep slopes, fail the correlation process and appear as no-data pixels. We patch these small discontinuous areas with the mean value of their surrounding pixels (using the FocalStatistics command in ArcMap), while larger collections of missing pixels are cropped out entirely. Other possible DEM artifacts usually manifest as seams in the data caused by slight differences across the charged coupled device (CCD) or as a "block" pattern caused by problems with the parameters set in the ASP algorithm (Kirk et al., 2008). These features can be difficult to remove (if reprocessing with different parameters is unable to create fewer errors). So, to avoid incongruous topographic analyses (e.g., sharp vertical jumps in elevation along artifact boundaries), we evaluate transects bounded within any artifacts.

To compare the resulting ASP elevation data with the traditionally cited shoreline levels (and across separately derived ASP built DEMs), we attempt to correct for absolute elevations. HiRISE data products are map projected and bundle adjusted in Integrated Software for Imagers and Spectrometers 3 before DEM creation and then subsequently referenced to the MOLA spheroid. Since ASP-derived stereo photogrammetry measurements yield MOLA ellipsoidal-referenced raster data rather than orthometric rasters, a correction must be applied for the deviation from the areoid (Mars geoid). MOLA PEDR points are overlaid onto a resampled (to the median value) DEM that matches the 300-m point shot resolution. Points where the resampled slope is greater than 15° are discarded. The elevation difference between the resampled topography and the MOLA PEDR points is then calculated, and outliers (>2 sigma) are also removed. An Inverse Distance Weighted interpolation function (third-order polynomial) is performed on the elevation difference points in ArcMap to create a surface raster that characterizes any cross-track "tilt" in the MOLA data. This resulting raster is then added to the areoid-subtracted DEM to form absolute elevations that are tied to MOLA elevation data. Total error on the absolute elevations is estimated at ±3.2 m based on an areoid error of at least ±3 m (Lemoine et al., 2001), individual shot point errors of ±1 m (Neumann et al., 2001), and an estimated ASP-derived DEM vertical precision of 0.3 m.

2.2.2. TEA

We employ the topographic signal processing techniques of Hare et al. (2001) which have been used successfully for identifying subtle, degraded, and topographically "noisy" (due in part to surface roughness) shoreline terraces on Earth (Hare et al., 2001; Jewell, 2016; Schide et al., 2018). Many of these subtle terrestrial paleoshorelines are difficult to discern with remote imagery, lidar, and field observations but can be clearly followed using this TEA on a high-resolution DEM (see Figures 2 and 13 of Jewell, 2016, for examples of identifying subtle shoreline features). Given the age of these hypothesized Martian paleoshorelines, it is expected that any preserved features would be subtle in their topographic signature expressions. While the TEA signal is not unique to paleoshorelines, it should be expressed by all erosional wave-generated paleoshoreline terraces when they exist in the geomorphology. Thus, we employ TEA as a key tool for testing whether putative wave-generated terrace features meet the topographic criteria necessary for paleoshoreline identification.

Given the challenges associated with recognizing and characterizing degraded wave-generated terrace features, analysis is done on the residual topography rather than the raw elevation data (Becerra et al., 2016; Hare et al., 2001; Head et al., 2002). The residual topography is the difference between the high-resolution DEM elevation data and an "idealized" local hillslope (one without terraces), highlighting where landforms deviate significantly from the overall slope and enhancing their morphological signal locally. By evaluating changes in the slope of the residual topography, subtle yet coherent geomorphic properties are illuminated. ArcMap's Trend tool is used to approximate the overall hillslope using a surface polynomial of varying degree (given the high number of potential shore/strandline features in each area, we elect for a high polynomial degree of 6). The approximated hillslope is then subtracted from the high-resolution DEM to create the residual topography raster.

In the residual topography raster, terraces appear as alternating light/dark bands of high and low residual topography making this process a quick litmus test as to whether the DEM shows evidence of laterally continuous features for additional investigation. Interpolated equally spaced residual-topographic profiles are created orthogonal to the strike of the follow-up hypothesized terraces. The first derivative (the slope of the residual) and the second derivative (changes in the slope) are also calculated to find the necessary inflection points of terraces. To reduce any "topographic noise" (e.g., from differential erosion or surface debris), a Savitsky-Golay filter is applied, via a MatLab script, to the residual topography profiles and their derivatives, which behaves similar to a moving-average filter. Choosing a window size and polynomial degree for the filter requires some experimentation to find a smoothing balance between data resolution and stability.

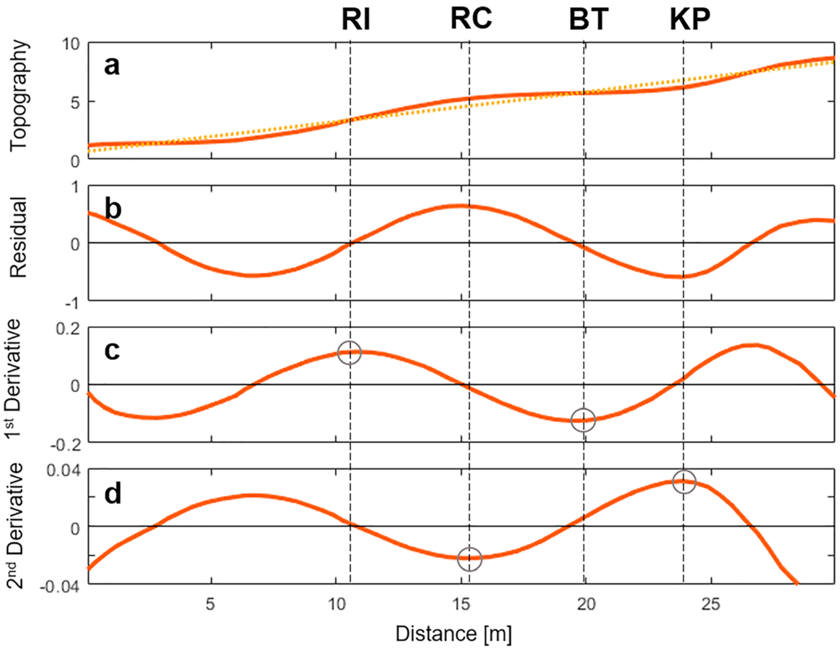

Figure 2. Topographic expression of an idealized paleoshoreline terrace after Hare et al. (2001) and Jewell (2016). (a) Solid line shows the topography of an arbitrary example terrace showing the riser inflection (RI), riser crest (RC), benchtop (BT), and knickpoint (KP). Dotted line shows a polynomial-fit "idealized" slope. (b) The residual topography taken from subtracting the idealized slope from the topographic data. (c) Smoothed first derivative of the residual topography where the circles represent defining the characteristic of RI and BT. (d) Smoothed second derivative of the residual topography where the circles denote the defining characteristic for RC and KP.

Decreasing polynomial degree or increasing filter increases the amount of smoothing. We opt for similar parameters used by Jewell (2016) as default, given the similar resolution between their lidar DEM and our stereo-derived DEM (i.e., a window size of ~11 m and a fourth-degree polynomial).

Terraces are identified by four components in the smoothed residual topography derivative products (Figure 2): the riser inflection (RI), marked by a maximum in the first derivative (max. slope) but only if there is a lower terrace, the riser crest (RC), marked by a minimum in the second derivative (max. concavity), the benchtop (BT), marked by minimum in the first derivative (the flattest part of the terrace), and the knickpoint (KP), marked by a maximum in the second derivative (max. convexity and break in the basal slope to the hillslope). The bench width is defined as the distance between the RC and the KP. Figure 2 summarizes the process for an arbitrary terrace feature and shows the characteristic behaviors of each residual derivative that define the terrace components.

If there are any paleoterrace landforms present in the profile, they will display these consecutive components (RI, RC, BT, and KP) even if they are degraded or subtle. Our MatLab script parses through the entire profile and outputs segments that fit the necessary criteria within a small epsilon value tailored to ignore insignificantly small maximum and minimum derivative values that correspond to any remaining topographic noise. While terrace features will exhibit this topographic behavior, there are other landforms that can appear as false positives. Thus, we manually inspected each identified segment for false positives (we also inspected for any terraces that were not identified by the TEA but found none).

Running this TEA for multiple (~20–30) transects along the hypothesized paleoshorelines allows for correlation of all quantitatively identified terrace features across the basin. Not only does this highlight whether the possible terraces follow the mapped contacts but creates standard reference points for comparing elevation data. We compared the calculated absolute elevation data of all found RC, BT, and KP to evaluate whether the identified terrace features follow an equipotential surface. Terrestrial shorelines can vary regionally in elevation by a few meters due to the local shorezone geometry (Atwood, 2006). Therefore, barring any significant geological activity (e.g., tectonic uplift or isostatic rebound) since their formation, shoreline contacts should appear within a narrow band of elevations approximating an equipotential surface. Noncoastal-origin terrace features (e.g., lithological units undergoing differential erosion) could also exist but would be expected to have a trend across the basin following any coherent dip in the lithology.

Additionally, the topographic profiles can be used in simple tests for typical shoreline geometries, such as the directionality of the slope. For example, lobate escarpments that face toward areas of high relief would be the opposite of what is expected in coastal zones (Malin & Edgett, 1999). Indeed, onlap of a deposit of some material up the marginal slope from the northern plains has been noted previously (Parker et al., 2010).

2.3. Thermal Inertia

Thermal inertia is a representation of a surface material's resistance to changes in temperature and its ability to conduct and store heat and thus provides important information about the bulk physical properties of the surface geology that cannot be acquired purely from images. Thermal inertia, I ($\mathrm{J{\cdot}m^{-2}{\cdot}K^{-1}{\cdot}s^{-1/2}}$ or thermal inertia units [tiu] from now on), is defined as $I \equiv \sqrt{\kappa \rho c}$ where κ is the thermal conductivity ($\mathrm{W{\cdot}m^{-1}{\cdot}K^{-1}}$), ρ is the density ($\mathrm{kg/m^3}$), and c is the heat capacity ($\mathrm{J{\cdot}kg^{-1}{\cdot}K^{-1}}$; e.g., Putzig & Mellon, 2007a).

Variations in thermal inertia on Mars are dominated by changes to κ, which are affected by the porosity, grain size, and induration (degree of cementation) of the surface material (κ can vary by up to a factor of 1,000, while ρc only varies by a factor of ~5 for Martian surface materials; Catling et al., 2006; Wood, 2011). Compositional differences due to changes in mineralogy have smaller effects on thermal inertia values. Given the range of factors that influence thermal inertia, it should be viewed as an approximate guide to a qualitative physical designation: Generally low values indicate mantling of loose fines (e.g., dust or very fine sand), intermediate values indicate cemented surfaces composed of sand-sized grains, and high values indicate rocky surfaces and bedrock. Uncemented dust-sized particles (<20 μm) coating the Martian surface could have thermal inertias up to ~170 tiu (Catling et al., 2006; Presley & Christensen, 1997), while values >1,200 tiu have been interpreted as bedrock (C. S. Edwards et al., 2009).

Thermal inertia maps can be used in identifying gradational grain-size boundaries that would be expected along shorezone contacts. The largest transportable sediments are generally located where wave energy is the highest, therefore if the coastal sediments are preserved and exposed, thermal inertia maps could show evidence of sediment sorting with grain size. Generally, the average grain size decreases landward (from the inshore to foreshore to backshore subzones; A. C. Edwards, 2001; Komar, 1998), and this may manifest itself as an increase in thermal inertia toward the highlands. These maps can also be used to analyze and identify potential constructional landforms versus underlying bedrock material and other heterogeneities that are useful for placing a genetic origin for uncertain morphological features (e.g., moraines or lava flows).

Global thermal inertia maps are available (e.g., Putzig & Mellon, 2007a), but we elect to create more finely tuned maps that better take into account local topography given the strong effects local slope and azimuthal orientation of the surface have on diurnal and seasonal surface temperature variations (Colwell & Jakosky, 2002; Putzig & Mellon, 2007b). We derive best-fit thermal inertia maps following the procedure of Sefton-Nash et al. (2012) and Catling et al. (2006) which use infrared (IR) images from the THEMIS (Christensen et al., 2004) and HRSC topography for each region.

The numerical thermal model generates lookup tables for spatially coincident THEMIS IR day and night images. These lookup tables provide synthetic diurnal surface temperatures as a function of topographic orientation (slope and azimuth angles), albedo, and thermal inertia for the THEMIS day-night images' latitude, solar longitude (season), and local time of day. Thermal inertia values are then determined by a best-fit least-squares analysis (Catling et al., 2006). Topographic data are primarily obtained from HRSC DEMs as opposed to the even higher-resolution HiRISE DEMs due to the small HiRISE footprint and incompatible fine resolution given THEMIS IR image resolution of ~100 m per pixel. MOLA topographic data (~400 m per pixel) are used where HRSC DEMs are unavailable or of poor quality. Full details of surface temperature retrieval methods are found in Sefton-Nash et al. (2012). THEMIS images are chosen to reduce possible attenuating effects (e.g., seasonal aerosols).

2.4. Spectroscopy

Differences in aqueous activity across potential paleocoastlines on Mars could be preserved in the surface mineralogical record as hydrous or aqueous alteration minerals. To investigate surface mineral composition, we use near-IR spectroscopic data obtained by the Compact Reconnaissance Imaging Spectrometer for Mars (CRISM) which operates at 0.36–3.92 μm sampled at 6.55 nm spectral resolution (Murchie et al., 2007). CRISM has multiple observation modes and, where available, we use the full resolution targeted (FRT) or the half-resolution targeted long/short (HRL/HRS) hyperspectral data at 18 and 36 m per pixel, respectively. However, in places where high-resolution spectral data are limited or nonexistent, we rely on the multispectral survey (MSP) data which has nearly global coverage at lower spatial and spectral resolutions (72 spectral bands at 200 m per pixel sampling).

Processing of CRISM spectral data is performed in a manner similar to Amador and Bandfield (2016) and Bandfield et al. (2013) using ENVI software (www.harris.com) and the CRISM Analysis Toolkit (available on the Planetary Data System [PDS]). Atmospheric gas absorptions are corrected for using the scaled volcano-scan method described in McGuire et al. (2009). Existing spectral index maps (as described in Pelkey et al., 2007, and Viviano-Beck et al., 2014) are used to rapidly assess evidence for key phase groups over an entire CRISM image. Follow-up on regions of interest in the spectral index maps is done by evaluating I/F values (CRISM incident radiance over the solar radiance at Mars distance divided by π) and spectral ratios of individual pixels. Spectral ratios are used to confirm the presence of spectral features by eliminating any systematic instrument error in the image. These spectral ratios are produced by dividing a pixel of interest's I/F value by the I/F value of a pixel considered spectrally neutral within the same image column.

Hydrated minerals display diagnostic absorption features between 1.1 and 2.65 μm (Carter et al., 2013). A variety of indices diagnostic of particular mineral features have been developed for CRISM data based on the band depth at a particular wavelength. For example, the D2300 index is sensitive to a negative drop in slope at 2.3 μm, characteristic of hydroxylated Fe/Mg-silicates, while the OLINDEX is sensitive to the broad Fe^{2+} absorption feature centered near 1.0 μm and is characteristic of olivine (possibly indicating unweathered basaltic minerals; Pelkey et al., 2007; Viviano-Beck et al., 2014). Additionally, we combine multiple indices to further constrain mineralogy such as how strong parameter values from both the BD1900 index (an indicator for bound H_2O) and the BD2210 index (which indicates Al-OH minerals) to determine the presence of Al-phyllosilicates.

Much of the surface of Mars is covered in a layer of fine dust, which has the potential to limit and interfere with spectral results. General circulation model results suggest that much of the northern plains represent a net erosive regime where fines have the potential to be removed (Haberle et al., 2003). However, dust coverage maps, based on observed surface properties, suggest a moderate level of dust along the topographic dichotomy with higher dust content in the northern lowlands (Ruff & Christensen, 2002). Therefore, spectral analysis of regions of interest may be impractical in many cases as the result of masking from fines or lack of adequate observations.

2.5. Classification

To assess the genetic origin of putative wave-generated paleoshoreline features with all available high-resolution images, we use the multifaceted approach outlined above. Given the data, each site can be classified as either (1) consistent with a paleoshoreline, (2) consistent with another origin (e.g., volcanic, glacial, impact, and mass wasting) and inconsistent with a paleoshoreline at a local and/or regional scale, or (3) indistinguishable with current data. While many formational processes produce similar features (e.g., lobate flows found in both volcanic and glacial settings), multiple lines of evidence are needed to classify a site to a specific genetic origin. Table 2 presents a list of the different data products used for the two sites in this study.

Given the wide range of possible morphologies, spectral properties, and unknown geologic history, there is no definitive list of expected features for paleoshorelines. So we evaluate all available evidence to assess whether suspected paleoshorelines show consistency regarding *photogeologic* evidence of erosional and/or depositional coastal landforms; *topographic* evidence in the form of TEA-defined terraces (if wave-generated landforms exist), lateral continuity of landforms across the basin, an equipotential surface (or following the regional trend if deformation occurred), shorezone slope; *mineralogic* evidence of some hydrous and aqueous alteration minerals, carbonates (McKay & Nedell, 1988; or possibly hydrous sulfates; Fairen et al., 2004); and *physical properties* such as grain-size sorting.

Table 2
Data Products Used for This Study

Instrument	Purpose	Western site	Res.	Southern site	Res.
HiRISE	Hi-res morphology, topography	ESP_025360_2165 ESP_025650_2165	0.3	PSP_001414_2165 PSP_001968_2165	0.5
CTX	Regional morphology	G18_025360_2168_XN_36N009W G19_025650_2167_XN_36N009W	7	B18_016789_2162_XN_36N009W	6
THEMIS	Thermal inertia maps	I04613003 I33546011	100	I14810020 I17936018	100
CRISM	Mineralogy	FRT_0002204A_07_IF167S	20	MSP000328B2_03_IF214L	200
HRSC	Coarse topography	H1216_0000	13	H1216_0000	13

Note. Image resolutions (res.) are provided in meters per pixel. HiRISE images and the western site CTX images are stereo pairs (resulting digital elevation models have resolutions comparable to the images). HiRISE = High Resolution Imaging Science Experiment (McEwen et al., 2007); CTX = Context Camera (Malin et al., 2007); THEMIS = Thermal Emission Imaging Spectrometer (Christensen et al., 2004); CRISM = Compact Reconnaissance Imaging Spectrometer for Mars (Murchie et al., 2007); HRSC = High Resolution Stereo Camera (Jaumann et al., 2007).

3. Results

3.1. Photogeology

3.1.1. Western Site Photogeology

The western site is dominated primarily by a degraded promontory that makes up the northern end of the breach between craters A and B (Figure 1). Figure 3a presents our mapped lineaments around the southern tip of this promontory that correspond to the putative shoreline contacts within the extent of the DEM elevation-corrected footprint. Clifford and Parker (2001) did not map lineaments here, but it represents a western continuation of their inferred shoreline with similar curvilinear features at the ~100-m spatial scale. The promontory is capped by a light-toned layer which was mapped and defined by Parker et al. (2010) as the Arabia level. There also appears to be a darker unit that mantled over the topography that has been stripped back.

Most of the curvilinear features in the visible imagery data were challenging to accurately map. Despite clear correlative features visible at the kilometer scale (Figure 3a), the spatial integrity of the features disappears at finer resolutions. Multiple lineaments bifurcate into additional features and/or truncate and grade into the surrounding material. This behavior makes it difficult to map the lineaments at the large scale for more than a few 100 m before they become convoluted with other lineaments or the surrounding mottled terrain.

Figures 3b–3d show sections of these putative shorelines at finer scales without the aid of the mapped lineament shapefiles. Here it becomes apparent that the individual lineaments lack any landform cohesion (recognizable as a single continuous distinct landform). The terrain these features are found in is predominantly composed of mottled terrain with some large boulders and blocks that tend to cluster around the mapped lineaments. As such, the lineaments appear as a roughened surface made up of disjointed blocky features with troughs cross-cutting the lineaments with no dominant preferred orientation and a lack of a coherent organization expected of drainage features. In many places, lighter-toned material is interposed between lineaments suggesting in some cases that these features are tonal lineaments with some lateral continuity representing material properties rather than landforms.

Lineaments are no longer visibly identifiable at the finer resolutions of Figure 3b. Instead, it appears there is a faint lighter-toned unit running through the center that loosely runs between the mapped lineaments. Note also the bifurcation on the east side of the image. Figure 3c shows a single clear identifiable lineament running NW-SE with additional smaller and fainter lineaments merging into it. The majority of features identified through the residual topography do not appear to map to any visible features in the visible image here. More arcuate lineaments are found in Figure 3d, though two merge in the NW corner and subsequently terminate. As seen at coarser scales, the southernmost lineament follows a shallow cliff. No constructional coastal terrain landforms or other erosional landforms is identifiable in the image.

3.1.2. Southern Site Photogeology

The southern site is characterized by a small embayment in the crater wall at the terminus of multiple valley networks (Figure 1). Figure 4 shows the historical mapped lineaments of Clifford and Parker (2001) with

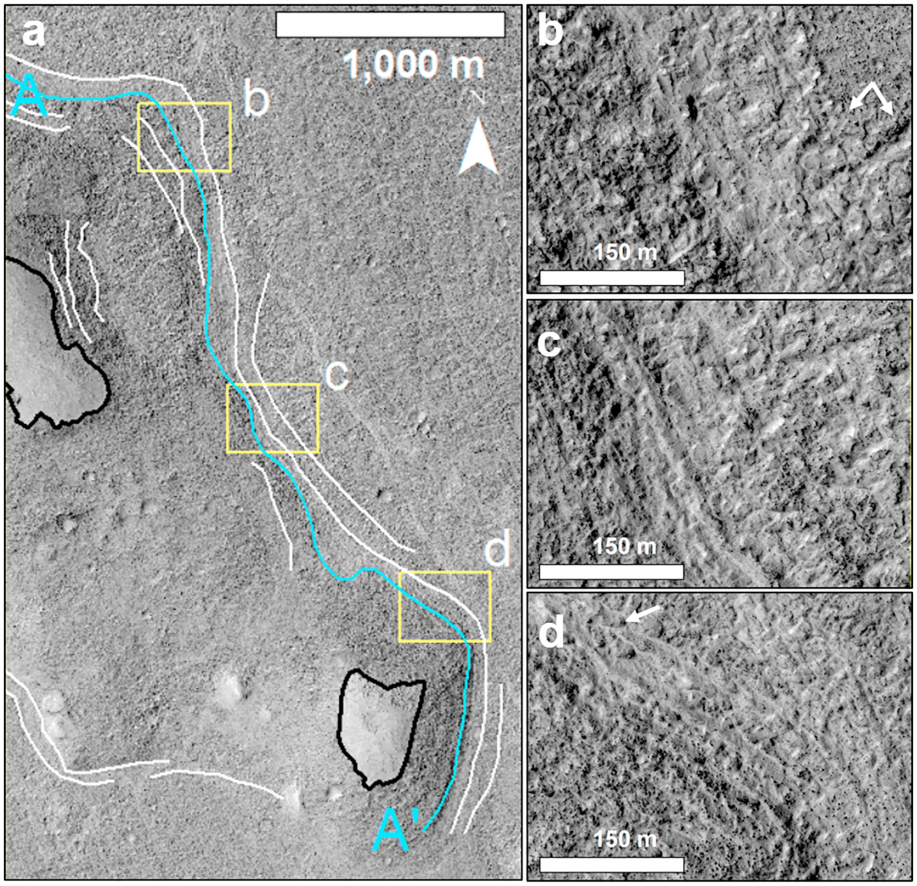

Figure 3. (a) Our mapped lineaments that follow the putative shoreline contacts for the western site of crater A. Topography for blue line A–A' is shown in Figure 5. Black lines map the lower contact of the smooth light-toned capping unit. Yellow rectangles show the locations of zoomed in areas displayed in (b)–(d). High Resolution Imaging Science Experiment image: ESP_025650_2165. Arrows in (b) show sides of a bifurcation, and the arrow in (d) show merging lineaments.

dotted lines, our mapped lineaments with solid thin lines, and lineaments observed only in the residual topography (see section 3.2.2) with dashed lines. Additional more pronounced lineaments are found in the CTX images to the west of the site, but we focus on the available high-resolution data. Parts of the dissected highland margin at the peak of the crater rim have eroded away into multiple alcoves (Świąder, 2014), some of which have short discontinuous lineaments corresponding to features mapped by Clifford and Parker (2001).

At coarse scales, the lineaments within the embayment are visible as shorter segments and difficult to trace as continuous features across the image. More pronounced lineaments are found to the east of the short promontory and are traceable for multiple kilometers. Unlike at the western site, bifurcation of the lineaments is not seen at these scales. However, most of the lineaments visually dissolve into the surrounding terrain at some point along trend. Mapping them thus involved some estimation.

The lineaments at finer scales behave similarly to those at the western site. Figure 4b exemplifies the lineaments as observed at the 100-m scale wherein clear visible linear trends in the terrain lack any clear landform continuity. The blocky nature of the lineaments at these scales makes it difficult to discern any continuity of the features and shows bifurcations and gradation into the surrounding terrain. Similar features displayed in Figure 4c also include bifurcations and merging of lineaments.

Analysis of the short discontinuous lineaments mapped by Clifford and Parker (2001) in the small alcove to the south (Figure 4d) shows highly disjointed segments that roughly follow short arcuate paths. Figure 4e

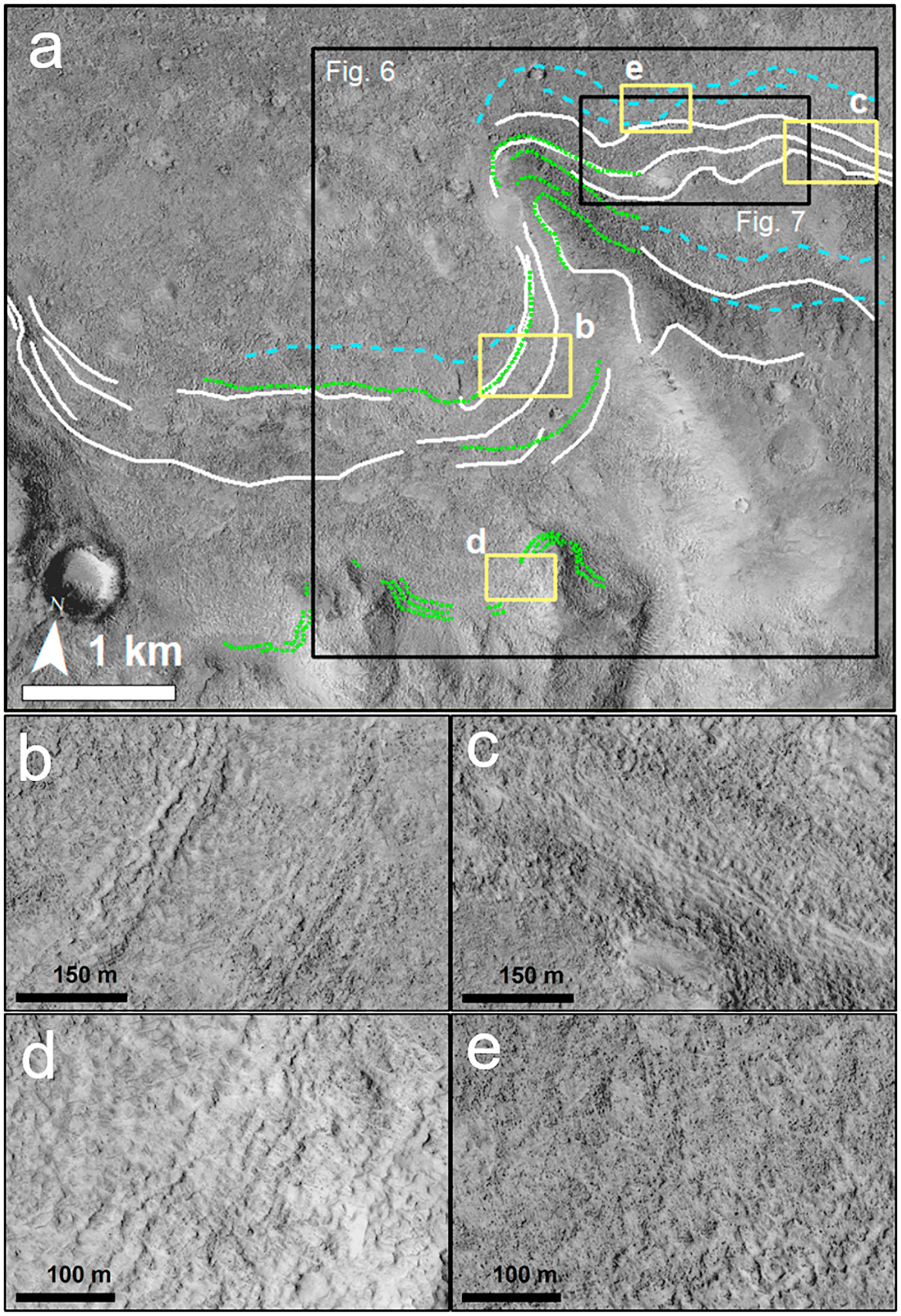

Figure 4. Mapped lineaments that follow the putative shoreline contacts for the southern site of crater A. Solid white lines demark lineaments that we mapped in the visible imagery; dashed blue lines demark additional lineaments resolved only in the residual topography data (see section 2.2.2); dotted green lines show mapped contacts by Clifford and Parker (2001). Yellow rectangles show the locations of zoomed-in areas displayed in (b)–(e). Black rectangles show extents for Figures 6 and 7. High Resolution Imaging Science Experiment image: PSP_001414_2165.

shows a section of the terrain where the residual topographic data (see section 3.2.2.) indicated a possible terrace landform. The terrain shows no visual lineaments and is dominated by the mottled terrain and boulders that appear as black specks at the scale of Figure 4e. At fine resolutions, lineaments that are apparent at coarse resolutions completely dissolve into the surrounding terrain and show no evidence for erosional or constructional landforms.

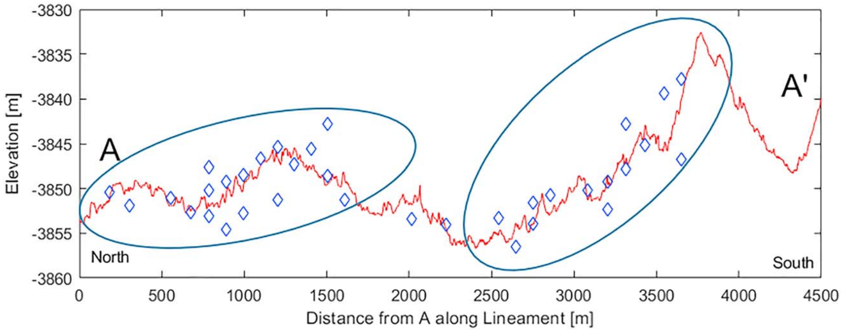

Figure 5. Along-track elevation data for curvilinear line A–A' in Figure 3 (solid blue line). Diamond markers indicate terraces found along profiles orthogonal to the lineament. Terraces appear to follow the topography rather than an equipotential surface. Ellipses outline clusters of terraces that appear to align with the topographic peaks of the promontory.

3.2. Topography

3.2.1. Western Site Topography

The residual topography map for the western site shows only two curvilinear bands for follow-up TEA. The upslope lineament shows long-scale continuity across the DEM footprint, while the other band is truncated to only ~500 m. The primary long-scale band follows the mapped lineament in Figure 3 and is also identifiable in the slope map as a sharp incline. TEA was applied to over 30 equally spaced 100-m topographic profiles (50 m to either side of the curvilinear line A–A′), and all but a quarter of them showed terrace expressions. The profiles that showed no terrace structures were primarily found in the central part of the mapped lineament creating two separate populations of terrace features. However, these terraces are widely varied in their morphologies (e.g., the shape and the width of the bench) with a handful of profiles showing multiple terraces at different elevations.

Plotting the elevation of the RCs and KPs (the start and end of the benches) as a function of latitude shows that both populations of terraces show a distinct downward tilt to the north (diamond markers in Figure 5). The southern population of terrace features show an elevation difference of ~20 m over ~1.25 km, while the northern population tilts ~10 m over ~1 km, but there is substantial variance in the distributions, with almost a 20-m range in elevations across all sites and up to about 10 m among proximal sites. The solid line in Figure 5 shows the elevations of the mapped lineament laterally. Mapping of the lineaments onto the CTX stereo pair shows a similar northern downward tilt of ~10 m/km. In contrast, we also mapped out the exposed contact of the light-toned capping unit of the promontory peaks. Fitting these elevations to a planar surface shows an approximate tilt of ~45 m/km to the south and ~30 m/km to the west.

The terraces appear to align with the topography rather than following an equipotential surface. Furthermore, the two populations of terraces tilt northward at different angles, while the unit stratigraphy appears to be tilting in the opposite direction (southward which itself is opposite than the general trend of the putative Arabia contact; Parker et al., 2010). Hence, the two terrace populations are likely manifestations resulting from the degradation of the promontory, which has created two peaks (corresponding to the smooth light-toned layer capping the promontory to the SE and WNW in Figure 3). Mapping the locations of the terraces with respect to their profiles along the lineaments highlights their discontinuous nature.

TEA was also performed for profiles along shorter truncated lineaments around the promontory. Some terraces were present in individual profiles, but the terraces could not be correlated along the lineaments and showed a highly discontinuous nature. The terraces that were identified only appeared when the topographic profiles were drawn across the blocks that make up the lineaments as was described with the HiRISE images. Analysis of the cliff at the southern tip of the promontory shows it is actually a series of shallow cliffs, ~2 m in height, that act as KPs in the slope with no terraces.

3.2.2. Southern Site Topography

At the southern site (Figure 4), topographic profiles across the putative shorelines in our high-resolution DEM show what appear to be multiple terrace features that visually resemble terrestrial wave-cut paleoshorelines. This is consistent with the findings of previous studies that have used the same stereo pair HiRISE images to conclude that the presence of terraces along these few profiles is consistent with a coastal origin

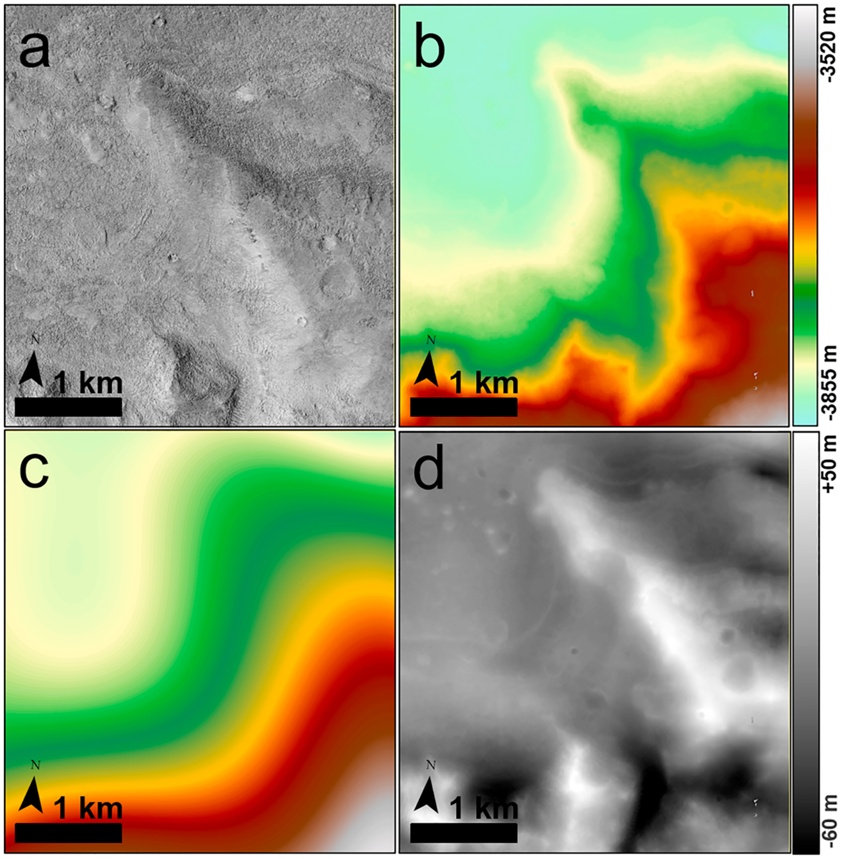

Figure 6. Steps of the topographic expression analysis on a subsection of the southern site. (a) Original High Resolution Imaging Science Experiment image, (b) our high-resolution digital elevation model, (c) surface polynomial fit surface representing an "idealized" slope, and (d) residual topography derived from subtracting the idealized surface from the topographic data. Potential paleoshoreline terraces appear as alternating dark/light bands in the residual topography. Further analysis of topographic transects is used to evaluate and eliminate false positives.

(Sholes et al., 2014; Śviąder, 2014). Figure 6 visually presents the process of our topographic expression analysis for the southern site which allows for a more thorough investigation into the extent of these terraces. This residual topography map identifies multiple possible terrace locations (appearing as alternating dark/light bands), including many that are too subtle to identify in the visible image.

The TEA code was performed along regularly spaced topographic profiles drawn orthogonal to the candidate terrace contacts found in the residual topography map. Figure 7a shows the locations of the terraces found that meet the necessary criteria for being a shoreline (i.e., having a recognizable RI, RC, BT, and KP in the residual derivatives) for five profiles on the east side of the southern site where the residual data were most pronounced. Manual inspection was performed across all profiles, as were sensitivity tests to explore the parameter space regarding the smoothing function (window size and polynomial degree) and the idealized slope (polynomial degree). These efforts found no convincing evidence for additional terrace features along the contact that were not found by the TEA code. The terraces found along the profiles range from −3,819 to −3,792 m in elevation (27 m of relief), using the MOLA-corrected absolute elevations. Half of them do not map to any lineaments found in the visible imagery, and most have a subdued expression with little to no lateral continuity.

Along these profiles, a collection of terraces (~7) were found clustered in a small region midway up the slope (shown in the lower part of Figure 7a) but do not appear spatially coherent as they do not map continuously along any visual lineament (either in the visual or residual data). Analysis of the local slope (Figure 7b) shows that these clustered terraces do not follow any continuous approximation of a flat surface bounded by sharp changes in slope that are normally associated with terraces. Rather, the slope map shows that

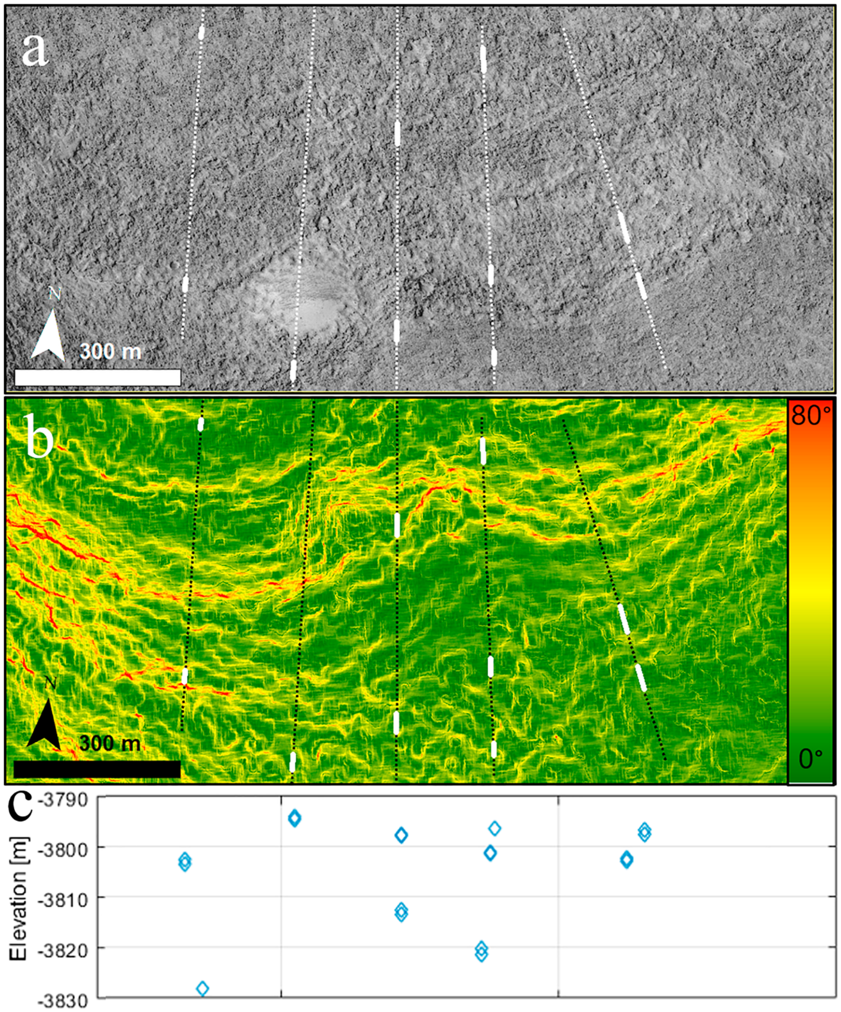

Figure 7. Locations of potential terraces (bold white segments) found along a sample of transects (dashed lines) orthogonal to the lineaments found in the surface residual topography. (a) High Resolution Imaging Science Experiment image, (b) slope map, and (c) corresponding elevations. Higher elevations are to the south in (a) and (b) and all terraces map vertically to their corresponding points in (c).

the terraces are bounded within individual small disjointed arcuate steep slopes. Elevation data (Figure 7c) agree, showing no consistent lateral trend across the terrace sites and >10-m range in topography.

The residual topography does highlight a pronounced subtle lineament that is not visible in the HiRISE imagery located (see Figure 4e) at the base of the crater wall slope. TEA analysis on the five profiles orthogonal to this feature confirms terraces along the lineament. An additional 30 transects were taken across this lower lineament to test for topographic continuity. Of these, transects 9 did not show the necessary criteria for a terrace, and the others showed a wide diversity in benchwidth and morphology. Evaluation of the elevations for the RCs and KPs finds that the along-strike trend of the terraces laterally is ~11 m downward to the east across the 2.5 km mapped stretch. Note that these terraces do not appear to follow any continuous landform and are not continuous in the slope map.

3.3. Thermal Inertia and Spectroscopy

There appears to be no consistent trend with the thermal inertia data across the contacts. The crater floor is relatively homogenous and characterized by thermal inertia values of ~400–550 tiu which we interpret as bedrock covered by a layer of sand or dust (Catling et al., 2006). The crater wall and highlands have thermal inertia values of ~300–350 tiu with some patches upward of ~450 tiu. These values are consistent with bedrock covered by a thin layer of poorly consolidated fines. Thermal inertia values of ~600–700 tiu are typically smaller craters and their associated ejecta with the exception of a lighter-toned boulder-free capping unit on the eastern site, which is interpreted as bedrock with a thin layer of dust. Thermal inertia maps can be found in Supporting Information S1.

High-resolution spectral/spatial CRISM data are only available for the western site. However, the site appears spectrally bland with a lack of mineralogical diversity. The derived visible and IR data products available on the PDS show stronger values in the VNIR_FEM (very near-IR Fe-minerals), with homogenous and bland in other relevant products (e.g., IR_HYD, IR hydrated mineralogy) suggesting the area is coated in dust (Viviano-Beck et al., 2014). Follow-up spectral ratios of individual pixels along transects orthogonal to the mapped contacts confirm the lack of nondust related spectroscopic signals.

4. Discussion

4.1. Are These Shorelines?

Along with the lack of clarity from the spectroscopic and thermal inertia maps, both the geomorphic and topographic data build a case that these lineaments at both sites are unlikely to be paleoshorelines or other ancient coastal features. At broad scales, the lineaments superficially resemble coastal ridges and strandlines, but at finer resolutions, identification of contacts is lost as they lack landform continuity in both the high-resolution visual and topographic data.

Degradation of paleoshorelines over geologic time (such as via periglacial or eolian destruction) can produce roughened texture and discontinuity at fine scales. However, at these fine scales and often in coarse scales, it becomes apparent that these features bifurcate, terminate, and merge. Identifiable terraces also do not line up with the lineaments, have no elevation or lateral coherence, and are limited in extent. These observations are incompatible with a preserved shoreline interpretation for the lineaments. Instead, the terrain appears to loosely follow material continuity along the degraded crater walls, as evidenced by multiple lighter-toned units interposed between the lineaments and clustering of boulders around the putative shorelines.

Topographic data agree with the visual geomorphic analysis. While terraces are found along certain topographic profiles (in agreement with previous studies), these are highly dependent upon the position and choice of such profiles. As the visual imagery suggests, the lineaments are made up of blocky material, and the terraces typically only appear when the profile crosses the blocks rather than the surrounding troughs. The TEA method we employ verifies that terrace features do exist but when applied to multiple profiles along a proposed contact confirms their lateral discontinuity. Many of the terraces are bounded by small disjointed arcuate steep slopes which we interpret to be slumped parts of the mottled terrain of the crater wall.

TEA was able to identify a single lineament at the southern site that had some topographically continuous terrace features. However, the morphology of the terraces varied widely, and nearly a third of the profiles did not have terraces that met the necessary criteria for interpretation as a shoreline. The terraces that were found along the lineament showed a consistent downward tilt of ~11 m (over ~2.5 km) to the east which is also inconsistent with unmodified shorelines. While the discrepancy of the westward ~60 m (over ~35 km) downward tilt between the eastern and southern site follows the long-wavelength topographic trends proposed as a result of true polar wander and/or flexure (Citron et al., 2018; Perron et al., 2007), the local trends of the putative shorelines tend in the opposite direction. Thus, at both scales, these features do not form an expected equipotential surface and likely represent separate features.

There is also no compelling evidence for constructional or erosional landforms at either site, a finding in agreement with the results of Ghatan and Zimbelman (2006), who used MOC narrow angle image data before HiRISE imagery was available. Given that these lineaments are found along the hypothesized Noachian-aged Arabia shoreline, it is expected that constructional landforms, typically composed of sand/pebble sized grains, would have eroded away, especially given the enhanced erosive rates of the Noachian (Carr & Head, 2010). The lack of any deltas or alluvial fans at the termini of the valley networks (located above the lineaments) suggests the reworking of the material and subsequent formation of the lineaments. Bedrock erosional landforms are expected to be better preserved, but impact gardening is expected to obscure any Noachian-aged shoreline features (erosional or otherwise) of $\lesssim$20 m (Hartmann et al., 2001).

4.2. Alternative Hypotheses

The lack of supporting geomorphic and topographic evidence does not necessarily preclude a paleoshoreline interpretation, as these lineaments could be highly degraded remnants of ancient coastal landforms that have undergone additional post-formational modification processes (to account for local tilting opposite the western Arabia level trend and the lack of an equipotential surface). However, there is no geomorphological evidence to suggest such a scenario, and compelling additional data would be required to accept such an interpretation.

An ocean on Mars is an extraordinary hypothesis that requires extraordinary evidence (because an ocean hypothesis raises questions of where the large volumes of water came from, where the water went, compatibility with geochemical tracers, consistency with past climates, and so on; e.g., Head et al., 2018). It has been said that "the most compelling evidence that Mars once had oceans is the presence of potential shorelines" (Zuber, 2018), so their reexamination is important. We propose that a much less speculative, conservative, and parsimonious explanation is that the lineaments that we have examined are likely the result of erosional degradation working on lithological differences in crater wall units. The blocky nature of the lineaments may be caused by differential erosion from thermophysical differences in interrock and intrarock units. This interpretation is in general agreement with the unit characteristics described by Tanaka et al. (2014) in which Noachian-aged material is commonly layered in crater walls.

These lineaments could also be the vestigial remnants of concentric crater fill (CCF) (Ghatan & Zimbelman, 2006) caused by ice-creep, eolian erosion, or debris-covered glaciers typically found at these midlatitudes (Fastook & Head, 2014). The bifurcations, terminations, troughs, and overall mottled terrain closely resemble the CCF "brain terrain" morphology of Levy et al. (2009, 2010, and references therein). These morphologies are common at the western site with the ridge and through structures and associated polygonal terrain at the crater base. Identification of the brain terrain morphologies also suffers from disagreements between scales, with contacts within the brain terrain ("open-cell" vs. "closed-cell") appearing as lineaments at large scales (Levy et al., 2010). However, this interpretation would also require invoking significant post-formational modification due to the lack of large areal debris aprons associated with CCF.

The long-scale tilting nature of the terrace features also supports a noncoastal interpretation. At these scales, it is unlikely that post-formational modification processes could account for the >60-m elevation displacements. Isostatic rebound is a proposed mechanism. However, the putative shoreline is circumferentially oriented (as opposed to radially) with respect to the basin center and only represents a small fraction of the Arabia contact both of which lessen the effect on the elevation variation (Currey, 1980; Webb, 2004). A simpler explanation is a shallow dip in the underlying rock layers.

5. Conclusions

We apply terrestrially validated topographic expression analysis (Hare et al., 2001; Jewell, 2016) to Mars for the first time as a more detailed quantitative approach to characterizing putative paleoshoreline features. We focused on an area in Cydonia Mensae that had been promoted as one of the better candidates for shorelines in the literature. Results from this analysis show neither elevational nor lateral coherence in identified terrace features. Additional high-resolution geomorphological analysis identifies inconsistencies between broad and fine scales with the lineaments, along with bifurcating along-trend behavior. Thus, we find that the lineaments identified within this crater complex are inconsistent with a wave-generated paleoshoreline interpretation. Rather, these lineaments appear to follow subtle discontinuous material-property boundaries.

Given both the highly localized nature of these features and their age, the lack of evidence for coastal landforms at this site does not preclude the existence of past oceans. Post-formational modification of any coastal landforms compounded over billions of years may erase any such geomorphic evidence. Additional work is required to apply the toolkit presented here to additional hypothesized shoreline contacts to assess their validity as coastal landforms and test the geomorphological evidence at a global scale. Furthermore, this toolkit can be applied elsewhere to characterize potential subtle paleoshorelines, such as on Titan given adequate topographic information.

Acknowledgments

We thank John Ferguson, Edwin Kite, and an anonymous reviewer for their supportive reviews, and we thank Tim Parker for a detailed critical review. We also thank Paul Jewell, Roger Buick, and Robert Pretlow for helpful discussions along with Elliott Sefton-Nash for help with the thermal inertia mapping code and Elena Amador for helpful discussions on CRISM spectral analysis. Arielle Michelman aided with data collection. Additional thanks to Oleg Alexandrov and David Shean for helpful guidance with the ASP software. S.F.S. and D.C.C. were partially supported by NASA Astrobiology Institute grant NNA08CN87A. Data used are listed in Table and available on the PDS. Mapped lineament shapefiles, MOLA-corrected DEMs, TEA MatLab scripts/ArcGIS toolbox, and TI data are accessible through the University of Washington ResearchWorks Archive (http://hdl.handle.net/1773/42764; Sholes, 2018).

References

Amador, E. S., & Bandfield, J. L. (2016). Elevated bulk-silica exposures and evidence for multiple aqueous alteration episodes in Nili Fossae, Mars. *Icarus*, *276*, 39–51. https://doi.org/10.1016/j.icarus.2016.04.015

Atwood, G. (2006). Shoreline superelevation: Evidence of coastal processes of Great Salt Lake, Utah. (thesis), Utah Geological Survey,

Baker, V. R., Strom, R. G., Gulick, V. C., Kargel, J. S., Komatsu, G., & Kale, V. S. (1991). Ancient oceans, ice sheets and the hydrological cycle on Mars. *Nature*, *352*(6336), 589–594. https://doi.org/10.1038/352589a0

Bandfield, J. L., Amador, E. S., & Thomas, N. H. (2013). Extensive hydrated silica materials in western Hellas Basin, Mars. *Icarus*, *226*(2), 1489–1498. https://doi.org/10.1016/j.icarus.2013.08.005

Banfield, D., Donelan, M., & Cavaleri, L. (2015). Winds, waves and shorelines from ancient Martian seas. *Icarus*, *250*, 368–383. https://doi.org/10.1016/j.icarus.2014.12.001

Bear, A. N., & Cas, R. A. F. (2007). The complex facies architecture and emplacement sequence of a Miocene submarine mega-pillow lava flow system, Muriwai, North Island, New Zealand. *Journal of Volcanology and Geothermal Research*, *160*(1-2), 1–22. https://doi.org/10.1016/j.jvolgeores.2006.09.002

Beaty, D. W., Clifford, S. M., Borg, L. E., Catling, D. C., Craddock, R. A., Des Marais, D. J., et al. (2005). Key science questions from the second conference on early Mars: Geologic, hydrologic, and climatic evolution and the implications for life. *Astrobiology*, *5*(6), 663–689. https://doi.org/10.1089/ast.2005.5.663

Becerra, P., Byrne, S., Sori, M. M., Sutton, S., & Herkenhoff, K. E. (2016). Stratigraphy of the north polar layered deposits of Mars from high-resolution topography. *Journal of Geophysical Research: Planets*, *121*, 1445–1471. https://doi.org/10.1002/2015JE004992

Boisson, J., Heggy, E., Clifford, S. M., Yoshikawa, K., Anglade, A., & Lognonne, P. (2011). Radar sounding of temperate permafrost in Alaska: Analogy to the Martian midlatitude to high-latitude ice-rich terrains. *Journal of Geophysical Research*, *116*, E11003. https://doi.org/10.1029/2010JE003768

Cabrol, N. A., & Grin, E. A. (1999). Distribution, classification, and ages of Martian impact crater lakes. *Icarus*, *142*(1), 160–172. https://doi.org/10.1006/icar.1999.6191

Carr, M. H. (1996). *Water on Mars*. New York: Oxford University Press.

Carr, M. H., & Head, J. (2019). Mars: Formation and fate of a frozen Hesperian Ocean. *Icarus*, *319*, 433–443. https://doi.org/10.1016/j.icarus.2018.08.021

Carr, M. H., & Head, J. W. (2003). Oceans on Mars: An assessment of the observational evidence and possible fate. *Journal of Geophysical Research*, *108*(E5), 5042. https://doi.org/10.1029/2002JE001963

Carr, M. H., & Head, J. W. (2010). Geologic history of Mars. *Earth and Planetary Science Letters*, *294*(3–4), 185–203. https://doi.org/10.1016/j.epsl.2009.06.042

Carr, M. H., & Head, J. W. (2015). Martian surface/near-surface water inventory: Sources, sinks, and changes with time. *Geophysical Research Letters*, *42*, 726–732. https://doi.org/10.1002/2014GL062464

Carter, J., Poulet, F., Bibring, J. P., Mangold, N., & Murchie, S. (2013). Hydrous minerals on Mars as seen by the CRISM and OMEGA imaging spectrometers: Updated global view. *Journal of Geophysical Research: Planets*, *118*, 831–858. https://doi.org/10.1029/2012JE004145

Castendyk, D., McKnight, D., Welch, K., Niebuhr, S., & Jaros, C. (2015). Pressure-driven, shoreline currents in a perennially ice-covered, pro-glacial lake in Antarctica, identified from a LiCl tracer injected into a pro-glacial stream. *Hydrological Processes*, *29*(9), 2212–2231. https://doi.org/10.1002/hyp.10352

Catling, D. C., Wood, S. E., Leovy, C., Montgomery, D. R., Greenberg, H. M., Glein, C. R., & Moore, J. M. (2006). Light-toned layered deposits in Juventae Chasma, Mars. *Icarus*, *181*(1), 26–51. https://doi.org/10.1016/j.icarus.2005.10.020

Chan, M. A., Jewell, P., Parker, T. J., Ormö, J., Okubo, C., & Komatsu, G. (2016). In C. G. Oviatt & J. F. Shroder (Eds.), *Pleistocene Lake Bonneville as an analog for extraterrestrial lakes and oceans*, *Developments in earth surface processes* (Vol. 20, pp. 570–597). Cambridge, MA: Elsevier. https://doi.org/10.1016/B978-0-444-63590-7.00021-4

Chan, N. H., Perron, J. T., Mitrovica, J. X., & Gomez, N. A. (2018). New evidence of an ancient Martian ocean from the global distribution of valley networks. *Journal of Geophysical Research: Planets*, *123*, 2138–2150. https://doi.org/10.1029/2018JE005536

Christensen, P. R., Jakosky, B. M., Kieffer, H. H., Malin, M. C., McSween, H. Y. Jr., Nealson, K., et al. (2004). The Thermal Emission Imaging System (THEMIS) for the Mars 2001 Odyssey Mission. *Space Science Reviews*, *110*(1/2), 85–130. https://doi.org/10.1023/B:SPAC.0000021008.16305.94

Citron, R. I., Manga, M., & Hemingway, D. J. (2018). Timing of oceans on Mars from shoreline deformation. *Nature*, *555*(7698), 643–646. https://doi.org/10.1038/nature26144

Clifford, S. M., Lasue, J., Heggy, E., Boisson, J., McGovern, P., & Max, M. D. (2010). Depth of the Martian cryosphere: Revised estimates and implications for the existence and detection of subpermafrost groundwater. *Journal of Geophysical Research*, *115*, E07001. https://doi.org/10.1029/2009JE003462

Clifford, S. M., & Parker, T. J. (2001). The evolution of the Martian hydrosphere: Implications for the fate of a primordial ocean and the current state of the Northern Plains. *Icarus*, *154*(1), 40–79. https://doi.org/10.1006/icar.2001.6671

Colwell, J. E., & Jakosky, B. M. (2002). Effects of topography on thermal infrared spectra of planetary surfaces. *Journal of Geophysical Research*, *107*(E11), 5106. https://doi.org/10.1029/2001JE001829

Currey, D. R. (1980). Coastal geomorphology of Great Salt Lake and vicinity. *Great Salt Lake: a scientific, historical and economic overview. Utah Geological and Mineral Survey Bulletin*, *116*, 69–82.

Di Achille, G., & Hynek, B. M. (2010). Ancient Ocean on Mars supported by global distribution of deltas and valleys. *Nature Geoscience*, *3*(7), 459–463. https://doi.org/10.1038/ngeo891

Edgett, K. S., & Parker, T. J. (1997). Water on early Mars: Possible subaqueous sedimentary deposits covering ancient cratered terrain in western Arabia and Sinus Meridiani. *Geophysical Research Letters*, *24*, 2897–2900. https://doi.org/10.1029/97GL02840

Edwards, A. C. (2001). Grain size and sorting in modern beach sands. *Journal of Coastal Research*, *17*(1), 38–52.

Edwards, C. S., Bandfield, J., Christensen, P., & Fergason, R. (2009). Global distribution of bedrock exposures on Mars using THEMIS high-resolution thermal inertia. *Journal of Geophysical Research*, *114*, E11001. https://doi.org/10.1029/2009JE003363

El Maarry, M. R., Markiewicz, W., Mellon, M., Goetz, W., Dohm, J., & Pack, A. (2010). Crater floor polygons: Desiccation patterns of ancient lakes on Mars? *Journal of Geophysical Research*, *115*, E10006. https://doi.org/10.1029/2010JE003609

Erkeling, G., Reiss, D., Hiesinger, H., Ivanov, M. A., Hauber, E., & Bernhardt, H. (2014). Landscape formation at the Deuteronilus contact in southern Isidis Planitia, Mars: Implications for an Isidis Sea? *Icarus*, *242*, 329–351. https://doi.org/10.1016/j.icarus.2014.08.015

Erkeling, G., Reiss, D., Hiesinger, H., Poulet, F., Carter, J., Ivanov, M. A., et al. (2012). Valleys, paleolakes and possible shorelines at the Libya Montes/Isidis boundary: Implications for the hydrologic evolution of Mars. *Icarus*, *219*(1), 393–413. https://doi.org/10.1016/j.icarus.2012.03.012

Fairen, A. G., Fernandez-Remolar, D., Dohm, J. M., Baker, V. R., & Amils, R. (2004). Inhibition of carbonate synthesis in acidic oceans on early Mars. *Nature*, *431*(7007), 423–426. https://doi.org/10.1038/nature02911

Fastook, J. L., & Head, J. W. (2014). Amazonian mid-to high-latitude glaciation on Mars: Supply-limited ice sources, ice accumulation patterns, and concentric crater fill glacial flow and ice sequestration. *Planetary and Space Science*, *91*, 60–76. https://doi.org/10.1016/j.pss.2013.12.002

Ghatan, G. J., & Zimbelman, J. R. (2006). Paucity of candidate coastal constructional landforms along proposed shorelines on Mars: Implications for a northern lowlands-filling ocean. *Icarus*, *185*(1), 171–196. https://doi.org/10.1016/j.icarus.2006.06.007

Goudge, T. A., Aureli, K. L., Head, J. W., Fassett, C. I., & Mustard, J. F. (2015). Classification and analysis of candidate impact crater-hosted closed-basin lakes on Mars. *Icarus*, *260*, 346–367. https://doi.org/10.1016/j.icarus.2015.07.026

Grotzinger, J. P., Gupta, S., Malin, M. C., Rubin, D. M., Schieber, J., Siebach, K., et al. (2015). Deposition, exhumation, and paleoclimate of an ancient lake deposit, Gale crater, Mars. *Science*, *350*(6257), aac7575. https://doi.org/10.1126/science.aac7575

Haberle, R. M., Murphy, J. R., & Schaeffer, J. (2003). Orbital change experiments with a Mars general circulation model. *Icarus*, *161*(1), 66–89. https://doi.org/10.1016/S0019-1035(02)00017-9

Hare, J. L., Ferguson, J. F., Aiken, C. L., & Oldow, J. S. (2001). Quantitative characterization and elevation estimation of Lake Lahontan shoreline terraces from high-resolution digital elevation models. *Journal of Geophysical Research*, *106*, 26,761–26,774. https://doi.org/10.1029/2001JB000344

Hartmann, W. K., Anguita, J., de la Casa, M. A., Berman, D. C., & Ryan, E. V. (2001). Martian cratering 7. The role of impact gardening. *Icarus*, *149*(1), 37–53. https://doi.org/10.1006/icar.2000.6532

Head, J. W., Forget, F., Wordsworth, R., Turbet, M., Cassanelli, J., & Palumbo, A. (2018). Two oceans on Mars? History, problems, and prospects. Paper presented at the 49th Lunar and Planetary Science conference.

Head, J. W., Kreslavsky, M. A., & Pratt, S. (2002). Northern lowlands of Mars: Evidence for widespread volcanic flooding and tectonic deformation in the Hesperian period. *Journal of Geophysical Research*, *107*(E1), 5003. https://doi.org/10.1029/2000JE001445

Hynek, B. M., Beach, M., & Hoke, M. R. (2010). Updated global map of Martian valley networks and implications for climate and hydrologic processes. *Journal of Geophysical Research*, *115*, E09008. https://doi.org/10.1029/2009JE003548

Irwin, R. P., Howard, A. D., & Maxwell, T. A. (2004). Geomorphology of Ma'adim Vallis, Mars, and associated paleolake basins. *Journal of Geophysical Research*, *109*, E12009. https://doi.org/10.1029/2004JE002287

Irwin, R. P., Maxwell, T. A., Howard, A. D., Craddock, R. A., & Leverington, D. W. (2002). A large paleolake basin at the head of Ma'adim Vallis, Mars. *Science*, *296*(5576), 2209–2212. https://doi.org/10.1126/science.1071143

Ivanov, M. A., Erkeling, G., Hiesinger, H., Bernhardt, H., & Reiss, D. (2017). Topography of the Deuteronilus contact on Mars: Evidence for an ancient water/mud ocean and long-wavelength topographic readjustments. *Planetary and Space Science*, *144*, 49–70. https://doi.org/10.1016/j.pss.2017.05.012

Jakosky, B. M., & Phillips, R. J. (2001). Mars' volatile and climate history. *Nature*, *412*(6843), 237–244. https://doi.org/10.1038/35084184

Jaumann, R., Neukum, G., Behnke, T., Duxbury, T. C., Eichentopf, K., Flohrer, J., Gasselt, S., et al. (2007). The High-Resolution Stereo Camera (HRSC) experiment on Mars Express: Instrument aspects and experiment conduct from interplanetary cruise through the nominal mission. *Planetary and Space Science*, *55*(7–8), 928–952. https://doi.org/10.1016/j.pss.2006.12.003

Jewell, P. W. (2016). Quantitative identification of erosional Lake Bonneville shorelines, Utah. *Geomorphology*, *253*, 135–145. https://doi.org/10.1016/j.geomorph.2015.09.022

Jöns, H.-P. (1985). Late sedimentation and late sediments in the northern lowlands on Mars. Paper presented at the 16th Lunar Planetary Science Conference, 414-415.

Kirk, R. L., Howington-Kraus, E., Rosiek, M. R., Anderson, J. A., Archinal, B. A., Becker, K. J., et al. (2008). Ultrahigh resolution topographic mapping of Mars with MRO HiRISE stereo images: Meter-scale slopes of candidate Phoenix landing sites. *Journal of Geophysical Research*, *113*, E00A24. https://doi.org/10.1029/2007JE003000

Komar, P. D. (1998). *Beach processes and sedimentation* (2nd ed.). Upper Saddle River, NJ: Prentice Hall.

Kraal, E. R., Asphaug, E., Moore, J. M., & Lorenz, R. D. (2006). Quantitative geomorphic modeling of Martian bedrock shorelines. *Journal of Geophysical Research, Planets*, *111*, E03001. https://doi.org/10.1029/2005JE002567

Kreslavsky, M. A., & Head, J. W. (2002). Fate of outflow channel effluents in the northern lowlands of Mars: The Vastitas Borealis Formation as a sublimation residue from frozen ponded bodies of water. *Journal of Geophysical Research*, *107*(E12), 5121. https://doi.org/10.1029/2001JE001831

Lammer, H., Zerkle, A. L., Gebauer, S., Tosi, N., Noack, L., Scherf, M., et al. (2018). Origin and evolution of the atmospheres of early Venus, Earth and Mars. *The Astronomy and Astrophysics Review*, *26*(1), 1–72. https://doi.org/10.1007/s00159-018-0108-y

Lemoine, F. G., Smith, D. E., Rowlands, D. D., Zuber, M., Neumann, G., Chinn, D., & Pavlis, D. (2001). An improved solution of the gravity field of Mars (GMM-2B) from Mars global surveyor. *Journal of Geophysical Research*, *106*, 23,359–23,376. https://doi.org/10.1029/2000JE001426

Levy, J. S., Head, J. W., & Marchant, D. R. (2009). Concentric crater fill in Utopia Planitia: History and interaction between glacial “brain terrain” and periglacial mantle processes. *Icarus*, *202*(2), 462–476. https://doi.org/10.1016/j.icarus.2009.02.018

Levy, J. S., Head, J. W., & Marchant, D. R. (2010). Concentric crater fill in the northern mid-latitudes of Mars: Formation processes and relationships to similar landforms of glacial origin. *Icarus*, *209*(2), 390–404. https://doi.org/10.1016/j.icarus.2010.03.036

Lucchitta, B. K., Ferguson, H. M., & Summers, C. (1986). Sedimentary deposits in the northern lowland plains, Mars. *Journal of Geophysical Research*, *91*, E166–E174. https://doi.org/10.1029/JB091iB13p0E166

Malin, M. C., Bell, J. F., Cantor, B. A., Caplinger, M. A., Calvin, W. M., Clancy, R. T., et al. (2007). Context camera investigation on board the Mars Reconnaissance Orbiter. *Journal of Geophysical Research*, *112*, E05S04. https://doi.org/10.1029/2006JE002808

Malin, M. C., & Edgett, K. S. (1999). Oceans or seas in the Martian northern lowlands: High resolution imaging tests of proposed coastlines. *Geophysical Research Letters*, *26*, 3049–3052. https://doi.org/10.1029/1999GL002342

Malm, J. (1999). Some properties of currents and mixing in a shallow ice-covered lake. *Water Resources Research*, *35*, 221–232. https://doi.org/10.1029/98WR02609

McEwen, A. S., Eliason, E. M., Bergstrom, J. W., Bridges, N. T., Hansen, C. J., Delamere, W. A., et al. (2007). Mars Reconnaissance Orbiter's High Resolution Imaging Science Experiment (HiRISE). *Journal of Geophysical Research*, *112*, E05S02. https://doi.org/10.1029/2005JE002605

McGuire, P. C., Bishop, J. L., Brown, A. J., Fraeman, A. A., Marzo, G. A., Morgan, M. F., et al. (2009). An improvement to the volcano-scan algorithm for atmospheric correction of CRISM and OMEGA spectral data. *Planetary and Space Science*, *57*(7), 809–815. https://doi.org/10.1016/j.pss.2009.03.007

McKay, C. P., & Nedell, S. S. (1988). Are there carbonate deposits in the Valles Marineris, Mars? *Icarus*, *73*(1), 142–148. https://doi.org/10.1016/0019-1035(88)90088-7

Mellon, M. T., Jakosky, B. M., & Postawko, S. E. (1997). The persistence of equatorial ground ice on Mars. *Journal of Geophysical Research*, *102*, 19,357–19,369. https://doi.org/10.1029/97JE01346

Moratto, Z. M., Broxton, M. J., Beyer, R. A., Lundy, M., & Husmann, K. (2010). Ames Stereo Pipeline, NASA's Open Source Automated Stereogrammetry Software. Paper presented at the 41st Lunar and Planetary Science Conference, 2364.

Mouginot, J., Pommerol, A., Beck, P., Kofman, W., & Clifford, S. M. (2012). Dielectric map of the Martian northern hemisphere and the nature of the plain filling materials. *Geophysical Research Letters*, *39*, L022022. https://doi.org/10.1029/2011GL050286

Murchie, S., Arvidson, R., Bedini, P., Beisser, K., Bibring, J. P., Bishop, J., et al. (2007). Compact Reconnaissance Imaging Spectrometer for Mars (CRISM) on Mars Reconnaissance Orbiter (MRO). *Journal of Geophysical Research*, *112*, E05S03. https://doi.org/10.1029/2006JE002682

Neumann, G. A., Rowlands, D. D., Lemoine, F. G., Smith, D. E., & Zuber, M. T. (2001). Crossover analysis of Mars orbiter laser altimeter data. *Journal of Geophysical Research*, *106*, 23,753–23,768. https://doi.org/10.1029/2000JE001381

Öhman, T. (2013). A beginner's guide to stereo-derived DEM production and analysis using ISIS, ASP, and ArcMap. *Lunar and Planetary Institute, internal report*. https://doi.org/10.13140/RG.2.1.1743.7609

Parker, T. J. (2004). A reassessment of the Mars ocean hypothesis. Paper presented at the 2nd Conference on Early Mars: Geologic, Hydrologic, and Climatic Evolution and the Implications for Life, 8085.

Parker, T. J., & Calef, F. J. (2012). Digital global map of potential ocean paleoshorelines on Mars. Paper presented at the Third Conference on Early Mars, 7085.

Parker, T. J., & Currey, D. R. (2001). Extraterrestrial coastal geomorphology. *Geomorphology*, *37*(3–4), 303–328. https://doi.org/10.1016/S0169-555X(00)00089-1

Parker, T. J., Gorsline, D. S., Saunders, R. S., Pieri, D. C., & Schneeberger, D. M. (1993). Coastal geomorphology of the Martian northern plains. *Journal of Geophysical Research*, *98*, 11,061–11,078. https://doi.org/10.1029/93JE00618

Parker, T. J., Grant, J., Anderson, F., & Franklin, B. (2002). MOLA topographic evidence for a massive Noachian ocean on Mars. Paper presented at the 33rd Lunar and Planetary Science Conference, 2027.

Parker, T. J., Grant, J. A., & Franklin, B. J. (2010). The northern plains: A Martian oceanic basin? In N. A. Cabrol & E. A. Grin (Eds.), *Lakes on Mars* (pp. 249–273). Boston: Elsevier. https://doi.org/10.1016/B978-0-444-52854-4.00009-X

Parker, T. J., Saunders, S. R., & Schneeberger, D. M. (1989). Transitional morphology in West Deuteronilus Mensae, Mars: Implications for modification of the lowland/upland boundary. *Icarus*, *82*(1), 111–145. https://doi.org/10.1016/0019-1035(89)90027-4

Pelkey, S. M., Mustard, J. F., Murchie, S., Clancy, R. T., Wolff, M., Smith, M., et al. (2007). CRISM multispectral summary products: Parameterizing mineral diversity on Mars from reflectance. *Journal of Geophysical Research*, *112*, E08S14. https://doi.org/10.1029/2006JE002831

Perron, J. T., Mitrovica, J. X., Manga, M., Matsuyama, I., & Richards, M. A. (2007). Evidence for an ancient Martian ocean in the topography of deformed shorelines. *Nature*, *447*(7146), 840–843. https://doi.org/10.1038/nature05873

Presley, M. A., & Christensen, P. R. (1997). Thermal conductivity measurements of particulate materials 1. A review. *Journal of Geophysical Research*, *102*, 6535–6549. https://doi.org/10.1029/96JE03302

Putzig, N. E., & Mellon, M. T. (2007a). Apparent thermal inertia and the surface heterogeneity of Mars. *Icarus*, *191*(1), 68–94. https://doi.org/10.1016/j.icarus.2007.05.013

Putzig, N. E., & Mellon, M. T. (2007b). Thermal behavior of horizontally mixed surfaces on Mars. *Icarus*, *191*(1), 52–67. https://doi.org/10.1016/j.icarus.2007.03.022

Ramirez, R. M., & Craddock, R. A. (2018). The geological and climatological case for a warmer and wetter early Mars. *Nature Geoscience*, *11*(4), 230–237. https://doi.org/10.1038/s41561-018-0093-9

Ruff, S. W., & Christensen, P. R. (2002). Bright and dark regions on Mars: Particle size and mineralogical characteristics based on Thermal Emission Spectrometer data. *Journal of Geophysical Research*, *107*(E12), 5127. https://doi.org/10.1029/2001JE001580

Schide, K. H., Jewell, P. W., Oviatt, C. G., Jol, H. M., & Larsen, C. F. (2018). Transgressive-phase barriers as indicators of basin-wide lake-level changes in late Pleistocene Lake Bonneville, Utah, USA. *Geomorphology*, *318*, 390–403. https://doi.org/10.1016/j.geomorph.2018.07.007

Sefton-Nash, E., Catling, D. C., Wood, S. E., Grindrod, P. M., & Teanby, N. A. (2012). Topographic, spectral and thermal inertia analysis of interior layered deposits in Iani Chaos, Mars. *Icarus*, *221*(1), 20–42. https://doi.org/10.1016/j.icarus.2012.06.036

Shean, D. E., Alexandrov, O., Moratto, Z. M., Smith, B. E., Joughin, I. R., Porter, C., & Morin, P. (2016). An automated, open-source pipeline for mass production of digital elevation models (DEMs) from very-high-resolution commercial stereo satellite imagery. *ISPRS Journal of Photogrammetry and Remote Sensing*, *116*, 101–117. https://doi.org/10.1016/j.isprsjprs.2016.03.012

Sholes, S. F. (2018). Quantitative High-Resolution Re-Examination of a Hypothesized Ocean Shoreline in Cydonia Mensae on Mars - Data Products. University of Washington ResearchWorks Archive. Retrieved from http://hdl.handle.net/1773/42764

Sholes, S. F., Catling, D. C., Pretlow, R., & Montgomery, D. R. (2014). High-resolution examination of the geomorphology of proposed ocean shorelines on Mars. Paper Presented at the 8th International Conference on Mars, Pasadena, CA, 1014.

Smith, D. E., Zuber, M. T., Frey, H. V., Garvin, J. B., Head, J. W., Muhleman, D. O., et al. (2001). Mars Orbiter Laser Altimeter: Experiment summary after the first year of global mapping of Mars. *Journal of Geophysical Research*, *106*, 23,689–23,722. https://doi.org/10.1029/2000JE001364

Som, S. M., Buick, R., Hagadorn, J. W., Blake, T. S., Perreault, J. M., Harnmeijer, J. P., & Catling, D. C. (2016). Earth's air pressure 2.7 billion years ago constrained to less than half of modern levels. *Nature Geoscience*, *9*(6), 448–451. https://doi.org/10.1038/ngeo2713

Squyres, S. W. (1979). The distribution of lobate debris aprons and similar flows on Mars. *Journal of Geophysical Research*, *84*, 8087–8096. https://doi.org/10.1029/JB084iB14p08087

Squyres, S. W., & Carr, M. H. (1986). Geomorphic evidence for the distribution of ground ice on Mars. *Science*, *231*(4735), 249–252. https://doi.org/10.1126/science.231.4735.249

Stüeken, E. E., Anderson, R. E., Bowman, J. S., Brazelton, W. J., Colangelo-Lillis, J., Goldman, A. D., et al. (2013). Did life originate from a global chemical reactor? *Geobiology*, *11*(2), 101–126. https://doi.org/10.1111/gbi.12025

Świąder, A. (2014). Identification and visualisation of possible ancient ocean shoreline on Mars using submeter-resolution digital terrain models. *Geologos*, *20*(4), 289–301. https://doi.org/10.2478/logos-2014-0017

Tanaka, K. L., Robbins, S. J., Fortezzo, C. M., Skinner, J. A., & Hare, T. M. (2014). The digital global geologic map of Mars: Chronostratigraphic ages, topographic and crater morphologic characteristics, and updated resurfacing history. *Planetary and Space Science*, *95*, 11–24. https://doi.org/10.1016/j.pss.2013.03.006

Tao, Y., Muller, J.-P., Sidiropoulos, P., Xiong, S.-T., Putri, A., Walter, S., et al. (2018). Massive stereo-based DTM production for Mars on cloud computers. *Planetary and Space Science*, *154*, 30–58. https://doi.org/10.1016/j.pss.2018.02.012

Villanueva, G. L., Mumma, M. J., Novak, R. E., Käufl, H. U., Hartogh, P., Encrenaz, T., et al. (2015). Strong water isotopic anomalies in the Martian atmosphere: Probing current and ancient reservoirs. *Science*, *348*(6231), 218–221. https://doi.org/10.1126/science.aaa3630

Viviano-Beck, C. E., Seelos, F. P., Murchie, S. L., Kahn, E. G., Seelos, K. D., Taylor, H. W., et al. (2014). Revised CRISM spectral parameters and summary products based on the currently detected mineral diversity on Mars. *Journal of Geophysical Research: Planets*, *119*, 1403–1431. https://doi.org/10.1002/2014JE004627

Walker, G. P. (1992). Morphometric study of pillow-size spectrum among pillow lavas. *Bulletin of Volcanology*, *54*(6), 459–474. https://doi.org/10.1007/BF00301392

Webb, V. E. (2004). Putative shorelines in northern Arabia Terra, Mars. *Journal of Geophysical Research*, *109*, 9010. https://doi.org/10.1029/2003JE002205

Wharton, R. A., Crosby, J. M., McKay, C. P., & Rice, J. W. (1995). Paleolakes on Mars. *Journal of Paleolimnology*, *13*(3), 267–283. https://doi.org/10.1007/BF00682769

Wood, S. E. (2011). A general analytic model for the thermal conductivity of loose, indurated or icy planetary regolith. Paper presented at the 42nd Lunar and Planetary Science Conference, 2795.

Zuber, M. T. (2018). Oceans on Mars formed early. *Nature*, *555*, 590–591. https://doi.org/10.1038/d41586-018-03415-x